ACS APPLIED MATERIALS & INTERFACES

Research Article

www.acsami.org

Joint Effects of Photoactive TiO_2 and Fluoride-Doping on SnO_2 Inverse Opal Nanoarchitecture for Solar Water Splitting

Yun Gun,[†] Gwang Yeom Song,[‡] Vu Hong Vinh Quy,[§] Jaeyeong Heo,[‡] Hyunjung Lee,[∥] Kwang-Soon Ahn,[§] and Soon Hyung Kang*[,⊥]

[†]Department of Chemistry Education, Chonnam National University, Gwangju 500-757, South Korea

[‡]Department of Materials Science and Engineering and Optoelectronics Convergence Research Center, Chonnam National University, Gwangju 500-757, South Korea

[§]Department of Chemical Engineering, Yeungnam University, Gyeongsan 712-749, South Korea

[∥]School of Advanced Materials Engineering, Kookmin University, Seoul 130-702, South Korea

[⊥]Department of Chemistry Education and Optoelectronics Convergence Research Center, Chonnam National University, Gwangju 500-757, South Korea

ABSTRACT: Inverse opal (IO) films of tin dioxide (SnO_2) were fabricated on polystyrene (PS) beads (diameter = 350 nm (±20 nm) with a spin coating method. To compensate for the large band gap (E_g = 3.8 eV), a thin TiO_2 shell was deposited on the SnO_2–IO films with atomic layer deposition (ALD), which produced shells with thicknesses of 10–40 nm. The morphological changes and crystalline properties of the SnO_2 and TiO_2-coated SnO_2 (herein after referred to as TiO_2/SnO_2) IO films were investigated with field-emission scanning electron microscopy and X-ray diffraction, respectively. The photoelectrochemical (PEC) behavior of the samples was tested in a 0.1 M KOH solution under 1 sun illumination (100 mW/cm^2 with an AM 1.5 filter). The highest PEC performance was obtained with the TiO_2(10 nm)/SnO_2 IO films, which produced a photocurrent density (J_{sc}) of 4.67 mA/cm^2 at 0.5 V (vs NHE) and was sequentially followed by the TiO_2(20 nm)/SnO_2–IO, TiO_2(30 nm)/SnO_2–IO, TiO_2 (40 nm)/SnO_2–IO and SnO_2 IO films. Overall, the thin TiO_2 shell covered on the SnO_2–IO core enhanced J_{sc} by 3 orders of magnitude, which in turn the PEC activity. This is mainly ascribed to the extremely low charge-transfer resistance (R_{ct}) in the photoelectrode/electrolyte and at the TiO_2/SnO_2 interface, as well as the contribution of the photoactive TiO_2 layer, which has an E_g of 3.2 eV. Moreover, to improve the electrical conductivity of the core SnO_2 IO film, the films were doped with 10 mol % of F. The F^- doped films were labeled as the FTO IO film. The R_{ct} of the FTO-IO films decreased because of the improved electronic conductivity, enhancing the PEC performance of the TiO_2(10 nm)/FTO-IO films by approximately 20%. The core–shell nanowire mesh nanoarchitecture is therefore suggested to provide an insight for designing the peculiar structure based on the material's properties and the engineering of their band gap energy for highly efficient PEC performance.

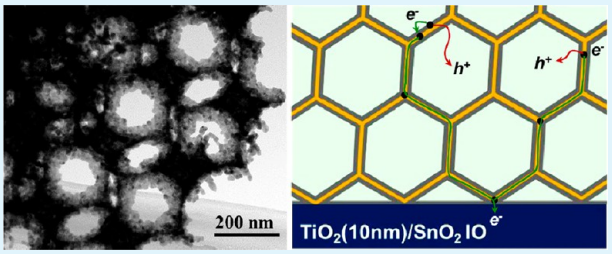

KEYWORDS: *SnO_2, TiO_2, core–shell inverse opals, photoelectrochemical water splitting, atomic layer deposition, F doped SnO_2*

1. INTRODUCTION

Since the first report on the photoelectrolysis of water by Fujishima and Honda,[1] the application of photoelectrochemical (PEC) water splitting as a type of solar energy conversion technique has gained significant interest where chemical fuels (e. g., O_2 and H_2 gases) can be generated by the photoelectrochemical reactions at the photoanode and photocathode when exposed to sunlight. A significant amount of attention has been focused in accordance with the international stream to pursuit the sustainable energy sources for the environmental benefit.[2−7] However, to commercialize the PEC water splitting, the photoconversion efficiency should be enhanced by at least 10% under the low developing charge.[8−10] In this regard, many diverse approaches and new materials have been recommended, and the fundamental interfacial phenomenon has also been studied to decrease the occurrence of side reactions.[11−13] Of these novel approaches and materials, the use of optimal materials for the given conditions has been regarded as a prime area where improvements can be made, because there are two basic conditions that must be met for water splitting reactions to occur: (1) the energetic band edges are suitable for the H_2O water splitting and (2) the materials are highly stable in aqueous solutions.[14−17] Accordingly, various potential materials have been surveyed and the first material tested was TiO_2 owing to its high photoactivity, low cost, and excellent chemical stability in aqueous solutions, as evaluated by Fujishima and Honda. However, the limiting factor for TiO_2 is its wide band gap (~3.2 eV), allowing the light harvesting only from the UV

Received: July 2, 2015
Accepted: August 31, 2015
Published: August 31, 2015

DOI: 10.1021/acsami.5b05914
ACS Appl. Mater. Interfaces 2015, 7, 20292−20303

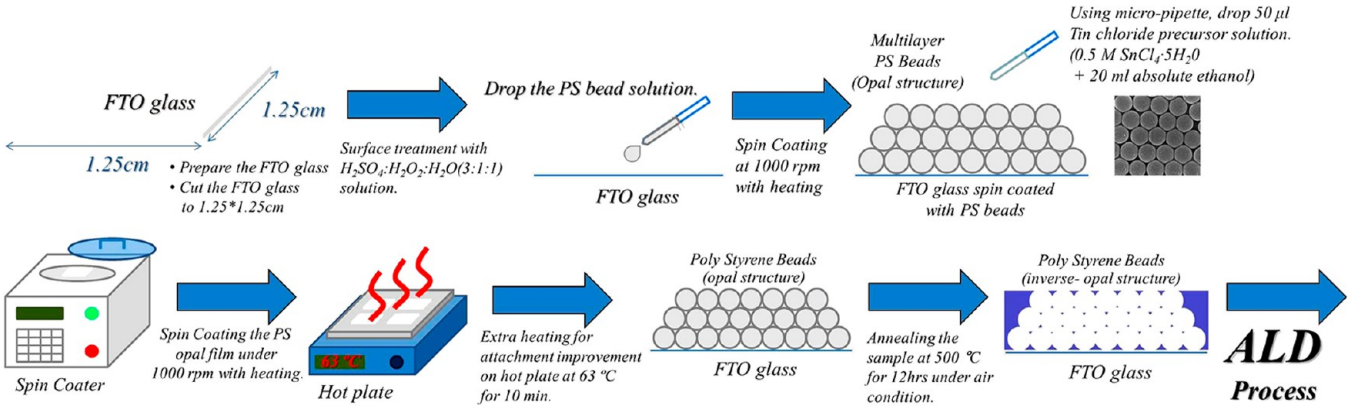

Figure 1. Schematic diagram showing the fabrication process for the TiO_2/SnO_2 IO nanostructures using a PS-bead template.

region. Thus, the heterogeneous structure between TiO_2 and other materials with visible-light absorbing ability has been suggested. Therefore, the development of quantum-dots or organic dye-sensitized PEC water splitting has resulted in a significant breakthrough with respect of the photoconversion efficiency up to 5.7%.[18,19] In other respect, many efforts have also been focused on modulating the microstructure (morphology, size, crystallinity, facets, etc.) of the photoelectrodes which affects the charge transport/transfer behaviors or reaction sites.[20−24] Nevetheless, the intrinsic charge transport properties of TiO_2 are still poor, leading to low conductivity of TiO_2 semiconductor. This causes significant charge recombination and charge trapping to occur during the charge migration toward the charge-collecting electrode. Therefore, the introduction of highly conductive photoelectrodes can be considered as a promising alternative for enhancing the effective movement of the photogenerated charge carriers. Both SnO_2 and F^- doped SnO_2 (FTO) exhibit superior electron mobilities (240 cm^2/V·s) of 2−3 orders of magnitude higher than that of TiO_2, and their conduction band (−4.66 eV) are approximately 300−500 mV lower than that of TiO_2.[25] Moreover, FTO not only has a highly electrical conductivity with a specific resistivity of 10^{-3} Ω·cm compared to that of SnO_2, but it also has a high transparency (>80%) in the visible-light region.[26] The type-II alignment between undoped- and doped-SnO_2 and TiO_2 may facilitate fast charge separation/transfer through the formation of core−shell SnO_2−TiO_2 or FTO-TiO_2 materials. Besides, SnO_2 has a small lattice mismatch with TiO_2, leading to good structural compatibility and stability.[27] Although the core−shell structure of the SnO_2−TiO_2 (denoted as TiO_2/SnO_2) is reported to decrease the exciton recombination, few studies have been reported.[28−30] In general, the performance of core−shell materials is known to be significantly affected by the properties of the shell such as the crystallinity and thickness. Despite the importance of the shell properties, the shell thickness dependent performance of TiO_2 shell in the TiO_2/SnO_2 nanoparticles has not yet been systematically studied.

Atomic layer deposition (ALD), a thin film deposition technique based on self-limiting surface reactions by sequential exposure of the substrate with different gas phase precursors, has been used to precisely modulate the deposited thickness at the atomic level. Furthermore, excellent step coverage with the high-aspect ratio is achieved for 3-dimentional (3D) nanostructure substrates by the ALD.[31,32] By using the ALD for the formation of the TiO_2 shell, the core−shell TiO_2−SnO_2 nanostructures may be formed uniformly and reproducibly, and the TiO_2 layer thickness can also be precisely controlled by varying the cycling number of the ALD.

The 3D nanowire mesh-type nanoarchitectures, called inverse opal (IO) structures, offer several advantages: (1) the large surface area, (2) favorable charge transport properties, and (3) photonic crystal effects, that contribute to the absorption of light. For example, a significantly improved PEC performance has been reported for 3D IO nanoarchitectures composed of Mo:$BiVO_4$, which is primarily due to the more effective charge collection and controllable macro- and meso-porosity.[33]

In this study, the TiO_2 shell layers of different thicknesses were deposited by the ALD on the surface of SnO_2-based 3D IO nanoarchitecture. Herein, the PEC performance significantly enhanced by tuning and optimizing the TiO_2 shell thickness owing to the synergistic effects of the superior charge transfer/transport, a large surface area, and effective photonic crystal effect. Furthermore, the introduction of the FTO IO instead of the SnO_2 IO further improved the PEC performance owing to its excellent electrical conductivity. The significantly enhanced PEC performances of the TiO_2/FTO core−shell IO structures were systematically studied in terms of charge separation, charge transport kinetics, recombination rate, electrochemical reaction, photonic crystal effect, and electrical conductivity.

2. EXPERIMENTAL SECTION

2.1. Preparation of the SnO_2 IO, FTO IO and TiO_2/SnO_2 IO Films. Figure 1 shows a schematic diagram of the simple method used to prepare the TiO_2/SnO_2 IO films. In brief, an FTO (Hartford Glass Corp., sheet resistance ∼15 Ω/sq.) substrate with a size of 1.25 × 1.25 cm^2 was prepared and cleaned via ultrasonication by sequentially immersing the substrate in ethanol, acetone, and distilled water for 20 min each. The substrate was then treated with a H_2SO_4:H_2O_2:H_2O (3:1:1, volume ratio) solution for 30 min to improve the hydrophilicity. An aqueous solution containing 10 wt % of polystyrene (PS) beads with an average diameter of 350 (±20) nm was prepared via emulsion polymerization, affording to an arranged face-centered cubic lattice (ABCABC). One drop of the PS bead solution was spread on the surface of the FTO substrate and subsequently spin-coated at 900 rpm for 10 s. The template consisting of the spin-coated PS beads was then dried at 70 °C for 20 min on a hot plate. An absolute-ethanol solution of tin tetrachloride ($SnCl_4$·5H_2O, 30 µL, 0.2 M) was dropped on the multilayered PS bead template. The $SnCl_4$·5H_2O solution subsequently infiltrated in the PS beads template, and any excess precursor solution was removed at a fast spin speed. After drying the sample for a short time, a high-temperature thermal treatment was performed at 500 °C for 3 h in air (ramping rate of 0.98 °C/min) to remove the PS beads template. For the FTO IO film on this template, the precursor solution consisting of 0.2 M $SnCl_4$·5H_2O containing 10

DOI: 10.1021/acsami.5b05914
ACS Appl. Mater. Interfaces 2015, 7, 20292−20303

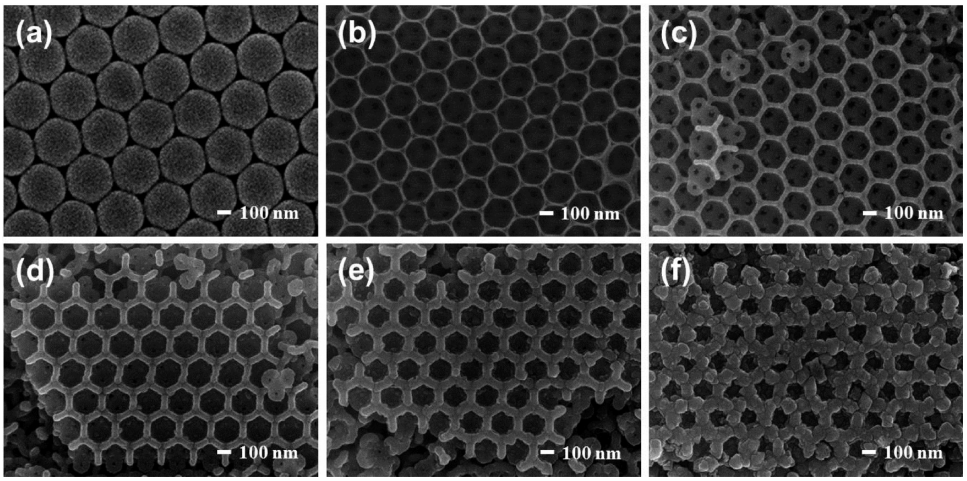

Figure 2. FE-SEM images of (a) 350 nm sized PS bead template, (b) SnO_2 IO, (c) TiO_2 (10 nm)/SnO_2 IO, (d) TiO_2(20 nm)/SnO_2 IO, (e) TiO_2(30 nm)/SnO_2 IO, and (f) TiO_2(40 nm)/SnO_2 IO film.

mol % of NH_4F was prepared, and the same experimental procedures to fabricate the SnO_2 films were followed. Finally, the SnO_2 and FTO IO films were placed in the ALD vacuum chamber to deposit the TiO_2 shells (thickness = 10 nm−40 nm). Titanium isopropoxide (Ti-{$OCH(CH_3)_2$}$_4$, UPChem. Korea) and deionized water were used as the sources of Ti and O, respectively, and the growth temperature was 250 °C. The initial growth rate of TiO_2 in ALD chamber is about 0.13 nm/cycles, subsequently increased to about 0.85 nm/cycle when the film thickness is thicker than 10 nm. The as-deposited thin TiO_2 shells exhibited an amorphous crystalline phase or weak crystallinity, and therefore, an additional annealing process was performed at 450 °C for 30 min under an air atmosphere to improve the crystallinity.

2.2. Characterizations. The PEC measurements were conducted in a three-electrode cell under light illumination using a potentiostat (CHI Instruments, USA). The SnO_2 and TiO_2/SnO_2 IO films were used as the working electrodes with an active area of 0.2 cm^2. A Pt sheet (area: 10 cm^2) and homemade Ag/AgCl electrode with saturated KCl (sat. Ag/AgCl with 0.11 V vs NHE) were used as the counter and reference electrodes, respectively. After nitrogen bubbling, an aqueous electrolyte containing 0.1 M KOH (pH 13.5) was used to remove the dissolved oxygen gas. The PEC responses were measured using a Xe lamp (150 W) with a light intensity of 100 mW/cm^2 with AM 1.5 filter. The current−voltage (J−V) performances under the chopped light on/off illumination were measured at a scan rate of 20 mV/s during the potential sweep. The incident photon-to-current conversion efficiency (IPCE) was measured in the wavelength range 300−500 nm at a potential of 0.5 V versus sat. Ag/AgCl electrode using a specially designed IPCE system for PEC water splitting. A 150 W xenon lamp was used as the light source for generating the monochromatic beam. The calibration was performed using an NREL-certified silicon photodiode.

Moreover, to evaluate the flat-band potential (V_{FB}) and donor concentration of the SnO_2 and FTO IO films, Mott−Schottky plots (AUTOLAB/PGSTAT, 128N) at a frequency of 1 kHz were measured using a standard potentiostat equipped with an impedance spectra analyzer (Nova) in the same electrochemical configuration and electrolyte under the dark condition. The electrochemical impedance spectroscopy (EIS) of the SnO_2 and TiO_2/SnO_2 IO films was measured in the same electrochemical configuration and electrolyte under 1 sun illumination condition. The frequency was measured in the range from 0.1 Hz to 10 kHz at an amplitude of ±10 mV. The thickness and morphology of the SnO_2, FTO, and TiO_2/SnO_2 IO films were confirmed by field-emission scanning electron microscopy (FE-SEM, S4800, HITACHI Inc.) operating at 10 kV and 20 mA. High-resolution transmission electron microscopy (HR-TEM, JSM-200FXII, JEOL, Japan) was also used to confirm the morphological and crystalline properties of the SnO_2, FTO, and TiO_2/SnO_2 IO films. The crystalline properties of the SnO_2, FTO, and TiO_2/SnO_2 IO films were investigated using a high-power X-ray diffractometer (HP-XRD, PANalytical, X'Pert PRO) operating at 40 kV and 30 mA. Furthermore, the transmittance of each sample was assessed using an ultraviolet−visible (UV−vis) spectrophotometer (LAMBDA-900 UV/VB/IR Spectrometer, PerkinElmer) in the wavelength range 300−800 nm.

3. RESULTS AND DISCUSSION

Figure 2 shows the top FE-SEM images of (a) PS bead template, (b) SnO_2 IO, (c) TiO_2 (10 nm)/TiO_2 IO, (d) TiO_2 (20 nm)/SnO_2 IO, (e) TiO_2 (30 nm)/SnO_2 IO, and (f) TiO_2 (40 nm)/SnO_2 IO films. The PS beads, which have an average diameter of 350 (±20) nm are well ordered in a regular close-packed sphere arrangement that corresponds to a face-centered cubic symmetry (ABCABC···). SnO_2 IO was visualized to be well connected between the neighboring pores, indicating that the spherical pores in the SnO_2 IOs are mostly in 3D ordered hexagonal close-packed array arrangement, preserving the original face-centered cubic arrangement of the PS beads templates. Based on the PS beads of 350 nm size, the pore shrinkage of ∼34% corresponded to a pore size of 230 (±10) nm, caused by the combination of the shrinkage of the polystyrene sphere during the thermal treatment for the template removal and the densification of SnO_2 during the phase transformation from the amorphous to the rutile phase.[34,35] Such shrinkage is similar to the reported values (25−30%) observed from the structures obtained by the sol−gel method.[36,37] A TiO_2 layer with an initially proposed thickness was uniformly deposited on 3D macroporous SnO_2 IO film by the ALD process. The pore diameter steadily decreased with increasing thickness of TiO_2 layer from 10 to 40 nm, and the pore diameter of TiO_2(40 nm)/SnO_2 IO film decreased to ∼130 nm, disclosing the distorted pore shape squashed by the thick TiO_2 layer. In contrast, the uniform pore ordering with the hexagonal shape was maintained for up to 30 nm-thick TiO_2-coated SnO_2 IO films. However, the wall thickness was found to be steadily increased by decreasing pore size with the increased thickness of TiO_2 layer. Overall, the basic skeleton of the IO film was still maintained despite of the deposited TiO_2 layer irrelevant to its thickness. To investigate the geometric change and morphological modification, the highly magnified FE-SEM images were recorded, as shown in Figure 3. From the pore diameter of 230 nm in the SnO_2 IO

DOI: 10.1021/acsami.5b05914
ACS Appl. Mater. Interfaces 2015, 7, 20292−20303

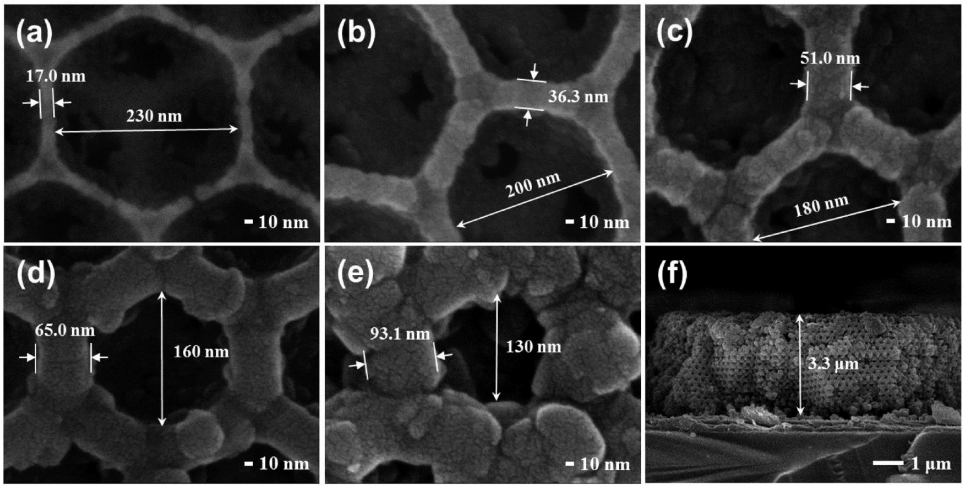

Figure 3. High-magnification FE-SEM images of (a) SnO_2 IO, (b) TiO_2(10 nm)/SnO_2 IO, (c) TiO_2(20 nm)/SnO_2 IO, (d) TiO_2(30 nm)/SnO_2 IO, (e) TiO_2(40 nm)/SnO_2 IO film, and (f) cross-sectional view of TiO_2(40 nm)/SnO_2 IO film.

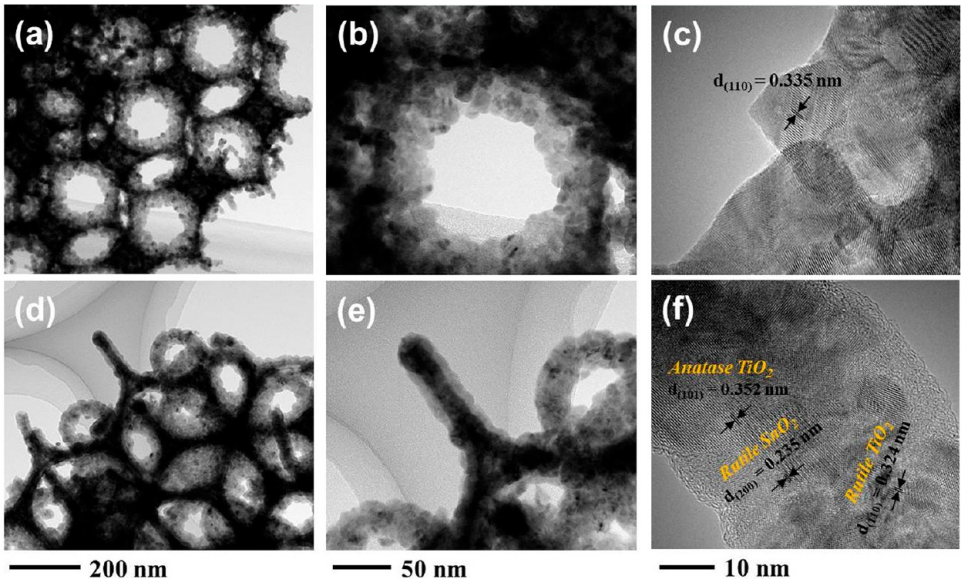

Figure 4. HR-TEM images of (a–c) SnO_2 IO and (c–e) TiO_2(10 nm)/SnO_2 IO.

film, the pore diameter sequentially decreased to 200 nm (TiO_2(10 nm)), 180 nm (TiO_2(20 nm)), 160 nm (TiO_2(30 nm)), and 130 nm (TiO_2(40 nm)). As a whole, the thickness of the TiO_2 layer increased by ~10 nm. In contrast, the wall thickness of the IO structure increased from 17 nm (SnO_2) to 93 nm (TiO_2(40 nm)), and the increasing ratio matched well with the initially proposed value. Overall, the systematic control of the TiO_2 thickness on the 3D nanowire mesh-type nanoarchitecture was possible by the ALD process. Moreover, a representative cross-sectional image of the 3.3 μm-thick TiO_2(40 nm)/SnO_2 IO film (Figure 3f) clearly shows that the TiO_2 layer is uniformly deposited on the inner side of the IO structure. In spite of a partially broken nanowire shells caused by the volume expansion of the opal template, a high degree of ordering in the SnO_2 IO film is also visible. To further investigate the core–shell structure, the HR-TEM measurements were performed for the SnO_2 IO and TiO_2(10 nm)/SnO_2 IO films, as shown in Figure 4. In the low-resolution view of the SnO_2 and TiO_2(10 nm)/SnO_2 IO films (Figures 4a,d, respectively), it is noteworthy that the inverse opal structure was comprised of the nanowire mesh skeleton where the small-size nanoparticles are tightly interconnected by the sol–gel process. Compared to the rough surface texture of the SnO_2 IO film, TiO_2(10 nm)/SnO_2 IO film shows the smoother surface morphology (Figure 4d), attributed to the recrystallization at the surface region of the SnO_2 IO film and the core–shell SnO_2–TiO_2 layer were remarkably distinguished by the contrast difference, and the conformal coating of TiO_2 was again identified through the entire area of SnO_2 IO film. Besides, a coating of 10 nm-thick TiO_2 layer is definitely visible (Figure 4e). In the high-magnification view on the surface region of IOs, the interplanar lattice spacing of 0.335 nm in the HR-TEM of the SnO_2 IO film (Figure 4c) with clear lattice fringes corresponded to the rutile (110) planes of SnO_2 crystal system. In contrast, TiO_2(10 nm)/SnO_2 IO film exhibits the rutile SnO_2 phase with an interplanar lattice spacing of 0.235 nm from (200) plane, the anatase TiO_2 phase corresponding to the (101) plane with the interplanar lattice spacing of 0.352 nm, and the rutile TiO_2 phase with the (110) plane accompanying with an interplanar lattice spacing of 0.324

DOI: 10.1021/acsami.5b05914
ACS Appl. Mater. Interfaces 2015, 7, 20292–20303

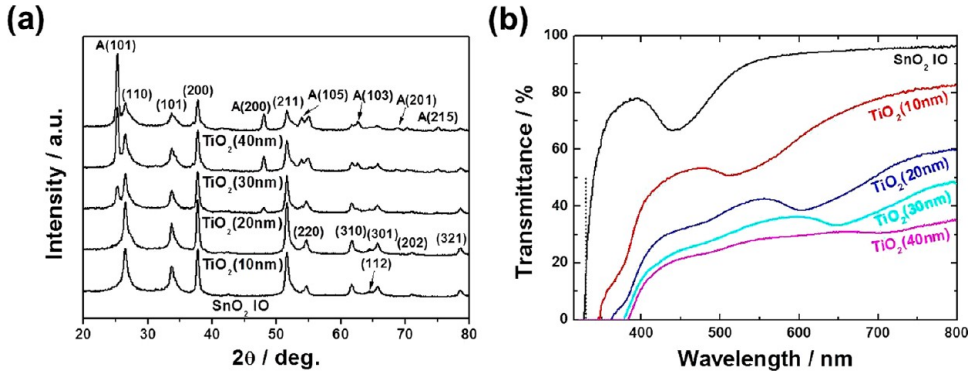

Figure 5. (a) XRD patterns and (b) UV−vis transmittance spectra of SnO_2 IO and TiO_2/SnO_2 IO films.

nm. Furthermore, the TiO_x amorphous phase is also partially observed in the shell region, probably resulting from the extremely thin film thickness. The rutile TiO_2 phase may be preferentially formed on the rutile SnO_2 phase, because the lattice mismatch between them approached to almost zero. However, the anatase TiO_2 phase was also formed despite of the significant lattice mismatch between them of >100%.[38−40] This is attributed to the high-temperature annealing treatment at 450 °C for 30 min under air, because the as-grown rutile TiO_2 phase with a very weak crystallinity or amorphous TiO_x phase can be easily transformed to the anatase phase. Taking into account that the anatase phase has a higher photoactivity than that of the rutile phase, the preferred formation of the anatase TiO_2 may enhance the PEC activity. The crystalline structure of the samples in the broad and in-depth range prepared with different TiO_2 thicknesses were characterized by XRD measurements, as shown in Figure 5. The highly polycrystalline rutile SnO_2 IO film was observed corresponding to the (110), (101), (200), and (211) planes. In the case of TiO_2(10 nm)/SnO_2 IO film, a very weak rutile TiO_2 phase is noticed at an angle of 27.5°, reflecting the presence of the rutile (110) plane on a basal rutile SnO_2 IO film. However, as the thickness of TiO_2 layer increased from 20 to 40 nm, the anatase TiO_2 peak with the (101) plane was dominantly observed instead of the rutile TiO_2 phase because the post-thermal treatment at high temperature (450 °C) easily transformed the anatase TiO_2 phase at 450 °C, and its intensity abruptly increased with increasing thickness of the TiO_2 layer. In contrast, even though the structure of SnO_2 IO skeleton is constantly maintained, the rutile SnO_2 peak of the (110) plane smoothly decreased, because of the decreased penetration depth of the X-ray beam through the TiO_2 layer. Furthermore, the deposition of a TiO_2 layer on the SnO_2 IO film induced the modification of the full-width at half-maximum of each curves, and the calculated average grain sizes of the SnO_2 IO film with the rutile (110) plane, TiO_2/SnO_2 IO film with the rutile (110) plane of SnO_2, and anatase (101) plane of TiO_2 are listed in Table 1. The pristine SnO_2 IO film exhibited an average crystalline size of 10.5 nm, whereas the crystallite size of SnO_2 IOs in TiO_2(10 nm)/SnO_2 IO film decreased to 8.73 nm. With increasing thickness of the TiO_2 layer, the SnO_2 crystallite size decreased and the TiO_2 crystallite size reversely increased. In fact, a certain stress can be achieved between the SnO_2 IO film with a wall thickness of ∼17 nm and at least 10 nm coating of the TiO_2 layer, depending on the lattice mismatch. In the case of rutile SnO_2 (a = 4.737 Å and c = 3.186 Å) and rutile TiO_2 (a = 4.584 Å and c = 2.953 Å) layers, the lattice mismatch was very small (3% for a-axis and 7% for c-axis), whereas the

Table 1. Average Crystallite Size of SnO_2 and TiO_2 Nanoparticles Composed of the IO Films and the Optical Bandgap of SnO_2 and TiO_2/SnO_2 IO Films

	crystallite size (nm)		
	SnO_2 (110)	TiO_2 (101)	E_g (eV)
SnO_2	11.9		3.8
TiO_2(10 nm)/SnO_2	8.73		3.44
TiO_2(20 nm)/SnO_2	8.77	11.0	3.34
TiO_2(30 nm)/SnO_2	6.62	15.8	3.29
TiO_2(40 nm)/SnO_2	4.70	16.7	3.24

combination of rutile SnO_2 and anatase TiO_2 (a = 3.784 Å and c = 9.515 Å) layers induced a large lattice mismatch of 20% (a-axis) and 198.6% (c-axis). Therefore, with increased thickness of the TiO_2 layer, the preferably formed anatase TiO_2 layer causes the tensile and compressive stress through the a- and c-axis, decreasing the size of the SnO_2 nanocrystals.[41] Despite a small lattice mismatch between the rutile SnO_2 and rutile TiO_2 layers, the union between the divergent materials affected their original thin films' characteristics, decreasing the average grain size. In contrast, the average crystallite size of the TiO_2 layer steadily increased by ∼16.7 at 40 nm thickness, because of the coalescence between the grains in the thin film during the annealing process. The effects of the grain size on the PEC water splitting have been reported in literature,[42] indicating that the increase in the grain size enhances the charge transport events, thereby directly contributing to the enhanced PEC performance. Therefore, the contradictory grain size between the SnO_2 and TiO_2 layers may play as a significant role on the PEC activity.

The optical and photonic band gaps of SnO_2 and TiO_2/SnO_2 IO films by collecting their transmittance using a UV−vis spectrophotometer were captured, as displayed in Figure 5b. In the case of the original SnO_2 IO film, the transmittance of >90% was attained in the wavelength range 600−800 nm, and the electronic band gap (E_g) was estimated to be ∼3.8 eV, as marked by the dotted line, accompanying the photonic band gap (PBG) of 2.82 eV from the light trapping at ∼440 nm. However, the absorption curve near the PBG is not symmetric, indicating the partial covering of the nonuniform IOs in the film.[43] In the case of the TiO_2/SnO_2 IO films, the transmittance steadily decreased in the wavelength region 600−800 nm, implicating a significant light absorption, reflection, and scattering. The wavelength of PBG was red-shifted with increasing thickness of the TiO_2 layer, almost approaching to 1.74 eV (TiO_2(40 nm)/SnO_2 IOs), pointing out that the light recognizes the mixed properties between SnO_2 and TiO_2

DOI: 10.1021/acsami.5b05914
ACS Appl. Mater. Interfaces 2015, 7, 20292−20303

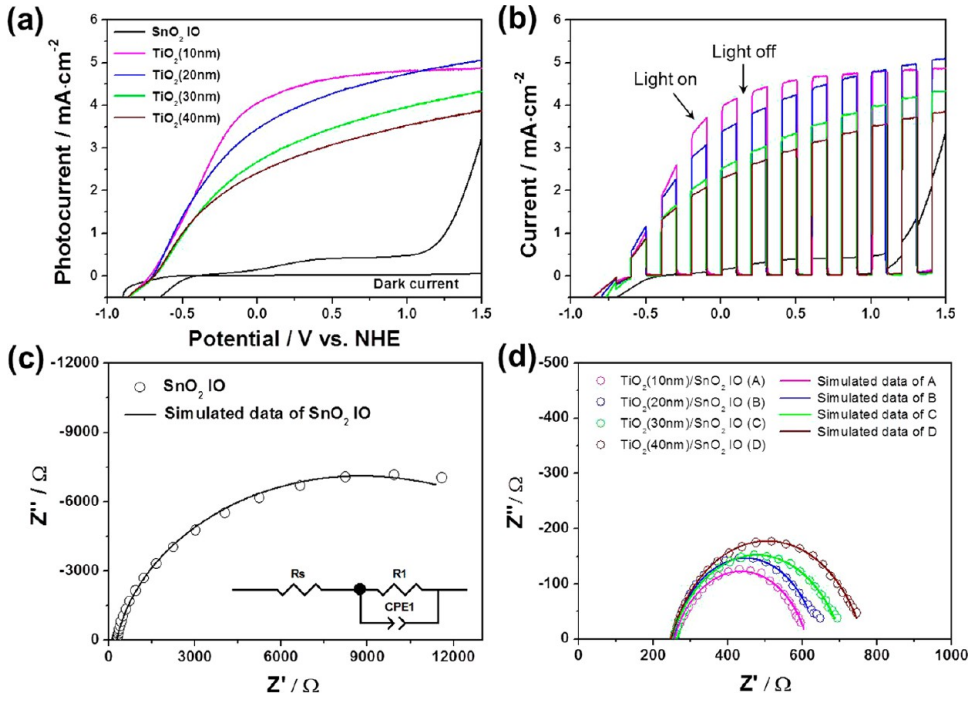

Figure 6. (a) LSV and (b) chopped LSV under full sun on/off cycles of SnO_2 IO and TiO_2/SnO_2 IO films in 0.1 M KOH solution and EIS spectra of (c) SnO_2 IO and (d) TiO_2/SnO_2 IO films under the solar illumination.

materials (not by TiO_2 or SnO_2 alone), and the TiO_2 layer can strongly affect the total materials' properties, probably because of the increased optical thickness (a unit of the repetitive cycle) of TiO_2−SnO_2−TiO_2 layer.[44,45] In the case of the SnO_2 IO film, the nanowire thickness of ∼17 nm is repetitively observed, whereas the thickness of the nanowires consisting of one SnO_2 and two TiO_2 layers in the TiO_2/SnO_2 IO film steadily increased as the TiO_2 thickness increased from 10 to 40 nm, increasing the thickness of the repetitive units. The increased optical thickness in the photonic crystal film red shifts the PBG, finally enhancing the light absorption in the longer wavelength region. Meanwhile, the intensity of the light absorption in the vicinity of the photonic band gap significantly decreased with increasing TiO_2 layer thickness, indicating the weakened photonic crystal effect, because of the abruptly decreased pore diameter and the damaged regular ordering of the IOs. The optical bandgaps (E_g) of the TiO_2/SnO_2 IO films was calculated from Figure 5b and are listed in Table 1. In comparison with the optical bandgap (3.8 eV) of the SnO_2 IO film, the E_g of the TiO_2/SnO_2 IO films decreased gradually with increasing thickness of the TiO_2 layer, reaching the E_g (3.2 eV) of the anatase TiO_2. This confirms that the mixed properties of SnO_2 and TiO_2 and the TiO_2 layer (versus the thin SnO_2 IOs) significantly affect the interaction of light, contributing gradually to the total optical band gap with increasing TiO_2 thickness. Therefore, the transformation of its optical property in the core−shell IOs electrode is feasibly dependent on the combination of materials and the adjustment of the thickness in each layer. Moreover, the light interacts concurrently with the mixed materials composed of the core−shell IO film, altering the photonic crystal effect.

Based on these materials, the PEC performances of the SnO_2 IO and TiO_2/SnO_2 IO films were measured in 0.1 M KOH solution under AM 1.5 G simulated sunlight illumination, as shown in Figure 6a,b. The linear-sweep voltammgrams (LSVs) in Figure 6a show the photoresponse (photocurrent density) in the range of the scanned potential at a scan rate of 20 mV/s. The dark current densities were measured for all the samples, indicating no apparent change. The representative dark current density acquired for the SnO_2 IO film under the dark condition (Figure 6a) was used to quantitatively estimate the photocurrent densities obtained under the illumination. Upon sweeping the potential from −1.0 to +1.5 V under the illumination, the SnO_2 IO film shows a significantly low photoresponse through the entire potential range with an onset potential of −0.51 V (vs NHE). Furthermore, the increasing rate (or steepness) of the photocurrent density after the onset potential is relatively low compared to those of other TiO_2/SnO_2 IO films. The SnO_2 IO film exhibited abruptly increasing photocurrent density from 1.0 V (vs NHE), owing to the tunneling effect by the band bending at the interfacial region between the SnO_2 IO film and electrolyte.[46,47] All the TiO_2/SnO_2 IO films exhibited similar onset potential of −0.8 V (vs NHE), indicating that the main photoactive reaction occurs by the TiO_2 shell layer, despite the very thin 10 nm-thick TiO_2 layer in the TiO_2(10 nm)/SnO_2 IO film. Because SnO_2 possesses a more positive conduction band edge in the range ∼300−500 mV than that of TiO_2, the positive shift in the onset potential of ∼300 mV confirms the formation of an intrinsic SnO_2 material. After the onset potential, the photocurrent density increased sharply for all the TiO_2/SnO_2 IO films, but the increasing rate gradually decreased as the TiO_2 layer thickness increased >10 nm. This can be attributed to the material resistance of TiO_2 itself. In the positive potential region showing saturated photocurrent density, the stable photocurrent was achieved in TiO_2(10 nm)/SnO_2 IO film, whereas the TiO_2/SnO_2 IO film with the thickness >20 nm shows no saturation of photocurrent, showing continuously increasing value with the increased potential. It may be attributed to the hindered charge transport in the TiO_2/SnO_2 IO films. As compared the photoresponse at the 0.5 V (vs NHE), TiO_2(10 nm)/SnO_2 IO film exhibited the highest values

DOI: 10.1021/acsami.5b05914
ACS Appl. Mater. Interfaces 2015, 7, 20292−20303

of 4.67 mA/cm^2, subsequently followed by 4.37 mA/cm^2 (TiO_2(20 nm)/SnO_2 IO), 3.57 mA/cm^2 (TiO_2(30 nm)/SnO_2 IO), 3.2 mA/cm^2 (TiO_2(40 nm)/SnO_2 IO) and 0.42 mA/cm^2 (SnO_2 IO). Taking into account the significantly low photocurrent density of the SnO_2 IO film, all the samples covered by the TiO_2 layer show the noticeable enhancement of at least seven times higher, and in particular, the TiO_2 (10 nm)/SnO_2 IO films show 10 times higher photocurrent density compared to the SnO_2 IO film. To evaluate how fast the charges are photogenerated or disappear, the chopped $J-V$ curves were measured under light on/off illumination at an interval of 5 s, as represented in Figure 6b. The tendency and quantitative values of the overall photocurrent density with the scanned potential are identical to those of the LSVs, and it also shows the abrupt production and extinction of the photogenerated charge under light on/off illumination, indicating fast charge transport for all the samples. That is, the composed medium (e.g., SnO_2, TiO_2, or the combined TiO_2/SnO_2) for the PEC water splitting offers the fast charge transport/transfer pathways.

To identify the electrochemically kinetic information happening at the each component and interfacial region in the PEC water splitting such as the charge transport in the photoelectrode or charge transfer at the photoelectrode/electrolyte, the EIS measurements were fulfilled at the frequency range from 10 kHz to 0.1 Hz at OCV under solar illumination. All the photogenerated electrons are recaptured by H^+ ions in the electrolyte before being extracted to the external circuit, and all the holes disappear by reacting with H_2O to produce O_2. Figure 6c,d shows the EIS spectra of the SnO_2 IO and TiO_2/SnO_2 IO films in 0.1 M aqueous KOH solution. To acquire the exact and quantitative values from each component, the equivalent circuit described in the inset of Figure 6c was facilitated for the simulation. The onset point on the real axis (R_s) at the high-frequency region represents the internal series resistance caused by the intrinsic components' resistance and the contact resistance between the photoelectrode and the substrate, which is ∼255 Ω. The diameter of the semicircle at the middle and low frequency regions is related to the interfacial charge transfer resistance (R_{ct}).[48] The SnO_2 IO film exhibited fairly large charge-transfer resistance (R_{ct}) of ∼23 000 Ω, whereas all the TiO_2/SnO_2 IO films exhibit significantly low R_{ct} values of ∼300−400 Ω, indicating that the photogenerated holes in the SnO_2 IO film experience ∼4 orders of magnitude higher bottleneck to reach at the electrolyte rather than that in the TiO_2 film of the TiO_2/SnO_2 IO films. Furthermore, considering that the maximum valence band edge of SnO_2 is positioned at −8.46 eV, the high overpotential can occur to make the holes transfer to the electrolyte for the water oxidation, leading to the significantly high R_{ct}. As well, it was well-known that the bulk SnO_2 has revealed several practical limitation due to short lifetime of the excited-state carrier (10^{-12} s), poor oxygen evolution reaction kinetics, and short hole diffusion length (2−4 nm). Therefore, the pristine SnO_2 IO film experienced the large R_{ct} for hole transfer to electrolyte.[49−52] The TiO_2/SnO_2 IO films (Figure 6d) show the sequential decrease in the R_{ct} values, corresponding well to the decreased thickness of the TiO_2 layer. TiO_2 is known to have a higher electrical resistance than SnO_2. The photogenerated electrons are formed mainly in the TiO_2 layer, followed by transferring to the SnO_2 core. However, the charge transporting pathways in the TiO_2 layer increased with increasing TiO_2 layer thickness, promptly increasing the R_{ct} at the interface between the SnO_2 and TiO_2 layers.

To investigate the enhanced photocurrent density in the TiO_2(10 nm)/SnO_2 IO film in more detail, the relationship between the photoactivity and the wavelength of the light absorption has to be investigated. Thus, the quantitative photoresponse as a function of the wavelength of the incident light was measured and plotted as incident photon-to-current conversion efficiency (IPCE). In this context, IPCE measurements were performed for the SnO_2, TiO_2(10 nm)/SnO_2, and TiO_2 (40 nm)/SnO_2 IO films at 0.5 V vs NHE in the 0.1 M KOH solution, as shown in Figure 7. The SnO_2 IO film showed

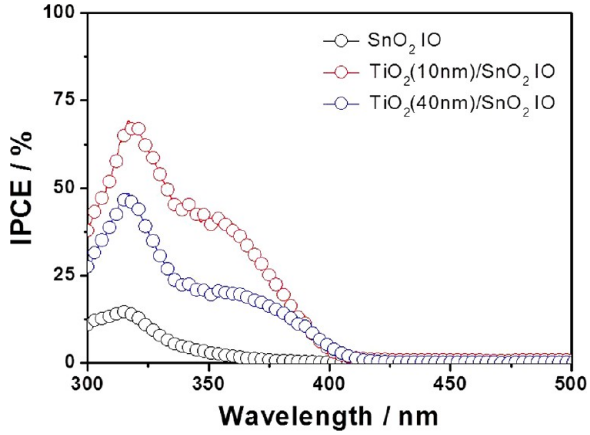

Figure 7. IPCE spectra of SnO_2 IO, TiO_2(10 nm)/SnO_2 IO, and TiO_2(40 nm)/SnO_2 IO film in 0.1 M KOH electrolyte.

the typical photoresponse of SnO_2 material, with a maximum IPCE of 14.7% at 315 nm and an onset potential of 385 nm. Moreover, the TiO_2/SnO_2 IO films exhibit two distinct peaks from the respective SnO_2 and TiO_2 layers and have similar overall IPCE patterns. The TiO_2(10 nm)/SnO_2 IO film showed the maximum IPCE value of 68.8% at 315 nm with a shoulder peak caused by the TiO_2 layer which has the 40.2% IPCE value at 350 nm, whereas the TiO_2(40 nm)/SnO_2 IO film shows the maximum IPCE value of 48.1% at 315 nm with the IPCE shoulder peak of 20.0% at 350 nm. The onset wavelengths of the TiO_2/SnO_2 IO films have the same wavelength as 420 nm owing to the light absorption of the TiO_2 layer. The IPCE can be expressed by the following equation:[53]

$$\mathrm{IPCE} = \frac{1239.8(\mathrm{W\cdot nm/A})J(\mathrm{mA/cm^2})}{\lambda(\mathrm{nm})J_{\mathrm{light}}(\mathrm{mW/cm^2})}$$

where J is the measured photocurrent density at a specific wavelength, λ is the wavelength of incident light, and J_{light} is the measured irradiance at a specific wavelength. The J_{sc} calculated by the integration of each IPCE spectrum was similar to J_{sc} at 0.5 V vs NHE in Figure 6. As a whole, the TiO_2(10 nm)/SnO_2 IO film exhibits the substantially enhanced photoactivity over the entire UV and near visible region, indicating that the high photoresponse can be obtained from the SnO_2 core, and the thin TiO_2 shell is composed of the IO film. Comprehensively, it is necessary to investigate the reason for the best PEC performance of the TiO_2(10 nm)/SnO_2 IO film relative to SnO_2 as well as the other TiO_2/SnO_2 IO films. Figure 8 depicts the simple schematic drawing to illustrate the charge generation and transfer/transport in the SnO_2 or core−shell SnO_2−TiO_2 nanowire mesh electrode with the band alignment between the

DOI: 10.1021/acsami.5b05914
ACS Appl. Mater. Interfaces 2015, 7, 20292−20303

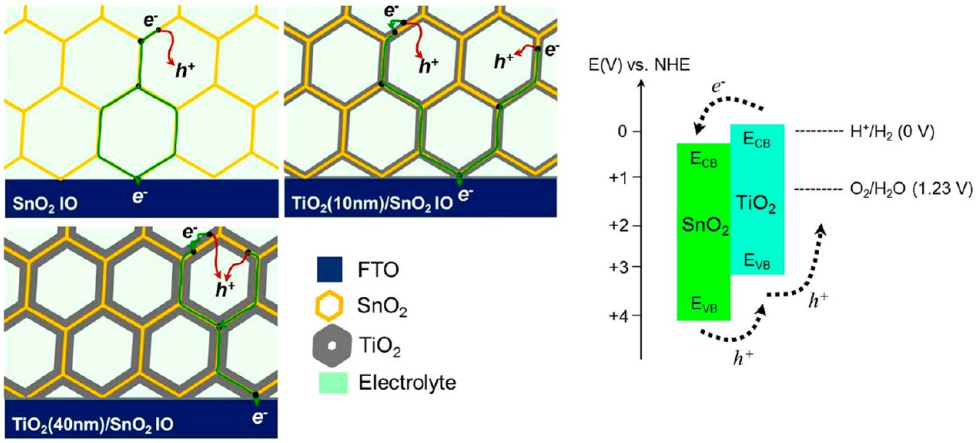

Figure 8. Simple schemes explaining the charge transfer events between SnO_2 IO and TiO_2 layer and its energetic band diagram at the interface between the SnO_2 IO and TiO_2 layer.

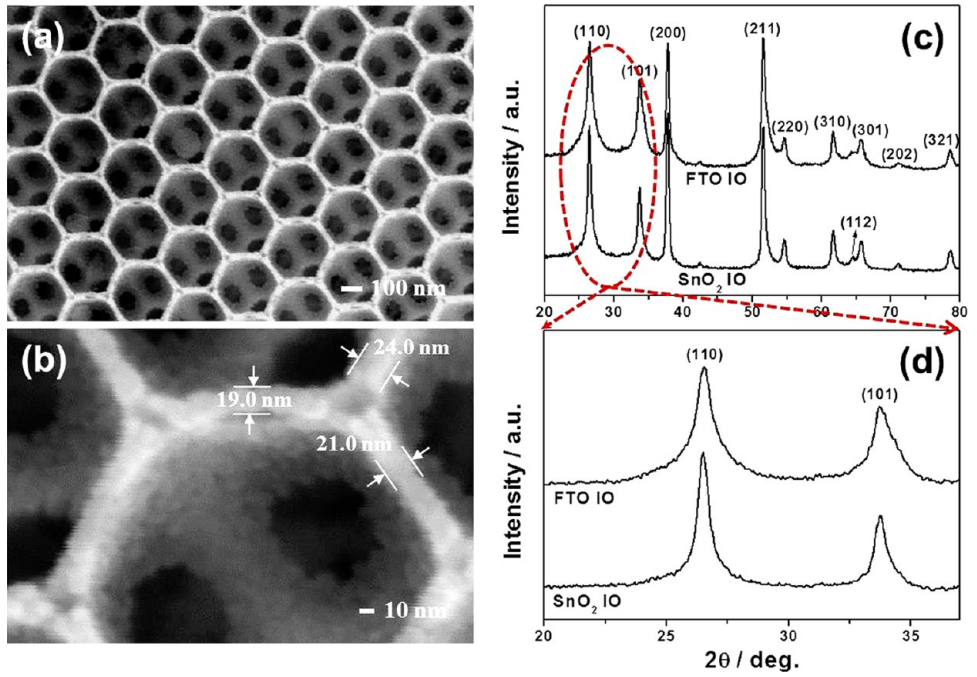

Figure 9. (a and b) FE-SEM images of the FTO IO nanostructure and (c and d) XRD patterns of the SnO_2 and FTO IO films.

TiO_2 and SnO_2 layer. First, the significantly enhanced J_{sc} of the TiO_2/SnO_2 IO films is owing to the low R_{ct} at the interfacial region from the TiO_2 surface and electrolyte, as compared to the SnO_2 IO film (already confirmed in Figure 6c). Furthermore, the intrinsic SnO_2 IO film possesses a wide E_g (3.8 eV) for the light absorption, causing the low light harvesting even in the UV region (Figure 5b). In contrast, the TiO_2(10 nm)/SnO_2 IO film exhibited significantly enhanced light harvesting by the TiO_2 shell layer corresponding to the SnO_2 IO film as a skeleton. However, in the case of core−shell nanowire mesh electrode, the charge transfer can occur at two sites including the interfacial region between the TiO_2 surface and electrolyte and between the TiO_2 shell and SnO_2 core layer. The former was already confirmed by the comparison of the R_{ct} between SnO_2 IO and TiO_2/SnO_2 IO films (Figure 6c). The latter can be certified by the changed R_{ct} value with the increased TiO_2 thickness. Figure 6d shows that the R_{ct} gradually increases with the TiO_2 layer thickness, because TiO_2 is more resistive for the electron transport than SnO_2, and, the photogenerated electrons can move from the TiO_2 shell to the SnO_2 core in the beneficial band alignment. During this process, the increase in R_{ct} because of the resistive TiO_2 can be developed with increasing TiO_2 layer thickness. Thus, the R_{ct} steadily increased for all the TiO_2/SnO_2 IO films. Furthermore, the decreasing average grain size of the SnO_2 IO film with increasing grain size of the TiO_2 IO (Figure 5a) may affect the charge transport, in which the charges generated in the large grain-sized nanoparticle can favorably transport to arrive at the charge collecting electrode. However, the decreased grain size of the SnO_2 core layer strongly suppresses the total charge transport rate, because most of charges move through the core SnO_2 layer which is fast charge transporting medium. In contrast, the TiO_2 coating may passivate the surface defects or trap sites of the SnO_2 IO film, blocking the charge recombination reaction at the interface region between the photoelectrode and electrolyte, contributing to the improved PEC Activity.[54−56] The apparent difference in the specific surface area between the samples was not found by the dye

DOI: 10.1021/acsami.5b05914
ACS Appl. Mater. Interfaces 2015, 7, 20292−20303

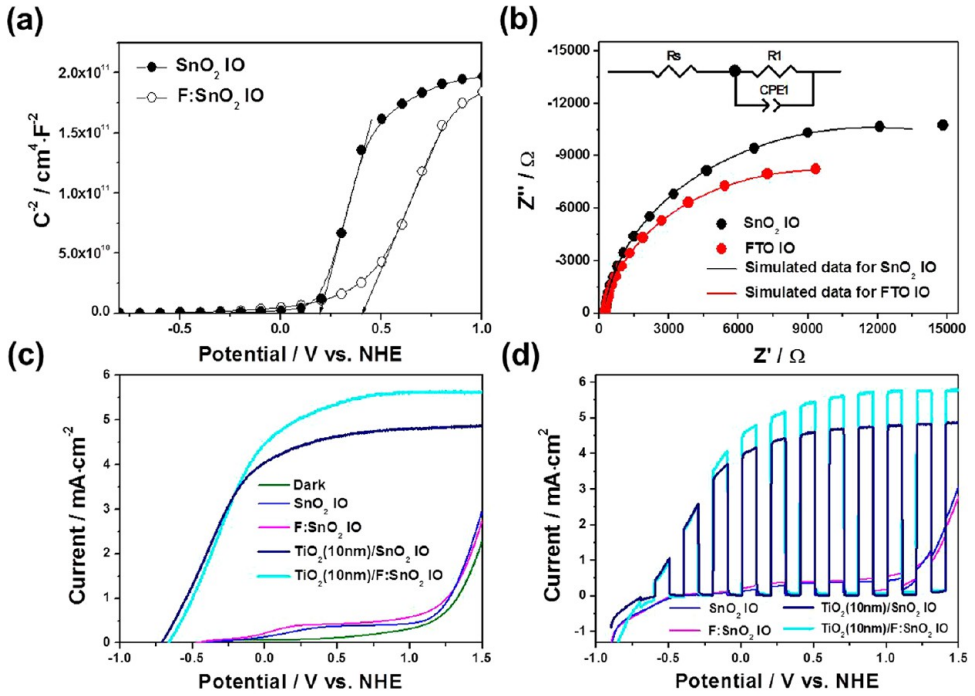

Figure 10. (a) Mott–Schottky plot in the dark condition, (b) EIS spectra under 1 sun condition (100 mW/cm^2 with AM 1.5) of the SnO_2 IO and FTO IO films, (c) LSV and (d) chopped LSV under 1 sun on/off cycles of the SnO_2 IO and FTO IO films in 0.1 M KOH solution.

desorption test in 0.1 M NaOH solution after the adsorption of N719 dye molecules in absolute ethanol (not shown here). The photonic crystal effect near the PBG in the SnO_2 and TiO_2/SnO_2 IO films hardly contributed to the improvement of the PEC performance, as confirmed by the IPCE spectra (Figure 7). Therefore, from this observation, the major enhancing factors of the TiO_2/SnO_2 IO films are the low R_{ct} and the increased light harvesting by the photoactive TiO_2 layer in the medium of highly conductive SnO_2 core.

To further enhance the PEC activity of the core–shell IO nanowire mesh electrode, the FTO IO films were employed by following the same experimental procedure except for the composition of the precursor solution composed of the 0.2 M $SnCl_4{\cdot}5H_2O$ containing NH_4F as a fluorine source (Sn:F = 9:1 mol %). Figure 9a,b show the top FE-SEM images of FTO IO structure well arranged in the hexagonal-closed packing. The pore diameter and wall thickness of the FTO IO film are about ~240 nm (±12 nm) and 21 nm (±3 nm), respectively. The FTO IO structure is almost identical to the pristine SnO_2 IO structure. To investigate the crystalline properties of SnO_2 and FTO IO films, the XRD measurements were performed, as shown in Figure 9c,d. Both the samples exhibit the typical polycrystalline rutile SnO_2 phase corresponding to the (110), (101), (200), (211), (220), (310), (301), (112), (202), and (321) planes with a high crystallinity. From the Scherrer's equation, the average crystallite size of both the samples was measured using the (110) peak, which are 11.9 and 6.7 nm for the SnO_2 and FTO IO films, respectively. Moreover, the (110) peaks are red-shifted from 26.52° (SnO_2 IOs) to 26.58° (FTO IOs), as presented in the Figure 9d, indicating that the F^- ions with a small ionic radius (1.17 Å) occupy substitutional sites of the O_2 with a large ionic radius (1.22 Å). This indicates that the inserted F^- ions in the SnO_2 precursor solution hinder the grain growth of the FTO during the sol–gel process.[57] Furthermore, the quantitative atomic percent of F content is about 1.6%, disclosing the extremely small amount, compared to the added weight percent of NH_4F from X-ray photoelectron spectroscopy, not shown here.

The effect of the F^- doping was also investigated electrochemically by the Mott–Schottky plots (M–S plots). Although the band bending is negligible for the nanoparticles with very small size below <6 nm, the band bending may be present in the nanoparticles with sizes >10 nm.[58,59] The nanocrystalline size of the SnO_2 and FTO IO films were in the range of ~10 nm, enabling them to form the space charge region. The Mott–Schottky plots involve the capacitance (C) of the space charge region as a function of the electrode potential. Thus, these provide the information on the carrier densities by the gradient $dV/d(1/C^2)$ of the M–S plots and the flat band potential (E_{fb}) by extrapolating the linear curve part to the y axis $(1/C^2) = 0$

$$N_d = \frac{2}{e_0 \varepsilon \varepsilon_0}\left[\frac{dV}{d(1/C^2)}\right]$$

where e_0 is the electronic charge, ε is the dielectric constant (170) of SnO_2, ε_0 is the permittivity of the vacuum, N_d is the donor density, and V is the applied voltage. Figure 10a shows the M–S curves of the SnO_2 and FTO IO films in 0.1 M KOH solution (pH 13) under the dark condition. The positive slope indicates that both the samples have n-type conductivity. From the magnitude of the slope, the calculated electron densities of the SnO_2 IO and FTO IO films were 2.35×10^{19} and 3.79×10^{19} cm^{-3}, respectively.[60,61] The FTO IO film showed ~60% higher donor densities than that of the SnO_2 IO film owing to the F^- doping and the presence of oxygen vacancies. Furthermore, the E_{fb} of the SnO_2 and FTO IO films were ~0.19 and 0.41 V vs NHE, respectively. The E_{fb} of the SnO_2 nanoparticles in 0.1 M Na_2SO_4 electrolyte was reported to be approximately ~0.32 V versus sat. Ag/AgCl electrode. The agreeable result was achieved in this IO system by the voltage conversion between different reference electrode scales as well

DOI: 10.1021/acsami.5b05914
ACS Appl. Mater. Interfaces 2015, 7, 20292–20303

as the potential shift by 59 mV/pH.[62] Compared to the E_{fb} of the SnO_2 IO film, the positive movement of the FTO IO film may be caused by the formation of lower quasi-Fermi level by the F^- doping. Moreover, the EIS spectra of the SnO_2 and FTO IO films were measured under the same experimental condition as the previous ones, as shown in Figure 6. To fit the EIS spectra quantitatively, the equivalent circuit added in the inset of Figure 10b was used. With the same R_s value (250 Ω), the R_{ct} (18200 Ω) of the FTO IO film abruptly decreased relative to that (23 000 Ω) of the SnO_2 IO film. The R_{ct} is mainly controlled by the transfer of the photogenerated holes between the photoelectrode and electrolyte, indicating that the material properties of the FTO IO film significantly facilitated the hole transfer to the electrolyte.

To compare the photoelectrochemical behavior of the SnO_2 and FTO IO films and the TiO_2(10 nm)- deposited SnO_2 and FTO IO films, the LSVs of the pristine SnO_2, FTO, TiO_2 (10 nm)/SnO_2 and TiO_2(10 nm)/FTO IO films under the 1 sun illumination and the LSV of SnO_2 IO film measured under the dark condition were shown in Figure 10c. The dark currents of the other samples were the same as that of the SnO_2 IO. The SnO_2 and FTO IO films exhibited only weak photoresponses (0.37 and 0.44 mA/cm^2 at 0.5 V, respectively). The FTO IO film showed slightly higher J_{sc} than that of the SnO_2 IO film, owing to the improved electrical conductivity of the FTO IO film and the beneficial charge transfer between FTO IO and the electrolyte as already confirmed in Figure 10a. The TiO_2 (10 nm)/SnO_2 and TiO_2(10 nm)/FTO IO films exhibited highly enhanced J_{sc} values in the entire potential region. In particular, the TiO_2(10 nm)/FTO IO film exhibited the significantly enhanced photoactivity of 5.46 mA/cm^2 at 0.5 V (vs NHE) compared to that (4.67 mA/cm^2 at 0.5 V vs NHE) of TiO_2(10 nm)/SnO_2 IO film. Approximately 17% enhancement was achieved by using the FTO IO film owing to the highly conductive pathway through the FTO core layer as identified by Figure 10a. Besides, Figure 10d shows fast charge generation and decay process in the FTO IO film when measured using the chopped on/off illumination. Overall, the F^- doping in the SnO_2 IO film improved the photoelectrochemical response up to ∼20% in the entire potential range. In particular, the TiO_2(10 nm)/FTO IO film exhibited the best J_{sc} value of 5.46 mA/cm^2, indicating the structural feasibility of the core−shell nanowire mesh electrode to obtain the high PEC performance and the modification of materials functionality based on their bandgap values.

4. CONCLUSIONS

Core−shell IO films, which are also called as core−shell nanowire mesh nanoarchitectures, were fabricated by either SnO_2 or FTO as the core and TiO_2 as the shell via a spin-coating method. The thickness of the TiO_2 layer was varied from 10 to 40 nm with ALD, and this layer functioned as the active photoresponse layer. When using a SnO_2 IO core, the TiO_2 (10 nm)/SnO_2 IO film exhibited the highest photoresponse of 4.67 mA/cm^2 at 0.5 V vs NHE, which was sequentially followed by the TiO_2(20 nm)/SnO_2 IO, TiO_2(30 nm)/SnO_2 IO, TiO_2(40 nm)/SnO_2 IO, and SnO_2 IO films. The main contributor to the high photoresponse is the tremendously low R_{ct} at the interface between the photoelectrode and electrolyte, as well as between the TiO_2 and SnO_2 layers, and the high light-harvesting efficiency offered by the photoactive TiO_2 shell and highly conductive SnO_2 core. Furthermore, the doping of the SnO_2 core layer with F increased the electrical conductivity in the core layer and decreased R_{ct} at the interface between the photoelectrode and electrolyte. Thus, the PEC response was significantly enhanced to 5.46 mA/cm^2 (vs NHE), which is an increase of approximately 20% compared to that of the TiO_2(10 nm)/SnO_2 IO film. These results suggest that the PEC performance can be dramatically improved by up to 3 orders of magnitude by introducing a thin TiO_2 shell to the 3D SnO_2 based IO nanoarchitecture. Thus, core−shell IO films may increase the PEC performance in terms of the functional structure and unification of the component materials via bandgap engineering.

AUTHOR INFORMATION

Corresponding Author

*E-mail: skang@jnu.ac.kr. Tel: +82-62-530-2497.

Notes

The authors declare no competing financial interest.

ACKNOWLEDGMENTS

This research was supported by the Basic Science Research Program of the National Research Foundation of Korea (NRF), which is funded by the Ministry of Science, ICT and Future Planning (Grant No. 2014R1A2A2A04004950). K.-S.A. would like to give thanks for the financial support provided by Basic Science Research Program through the National Research Foundation of Korea (NRF) funded by the Ministry of Education (NRF-2015R1D1A3A01016158).

REFERENCES

(1) Fujishima, A.; Honda, K. Electrochemical Photolysis of Water at a Semiconductor Electrode. *Nature* **1972**, *238*, 37−38.

(2) Li, Y.; Zhang, J. Z. Hydrogen Generation from Photoelectrochemical Water Splitting Based on Nanomaterials. *Laser Photonics Rev.* **2010**, *4*, 517−528.

(3) Townsend, T. K.; Sabio, E. M.; Browning, N. D.; Osterloh, F. E. Improved Niobate Nanoscroll Photocatalysts for Partial Water Splitting. *ChemSusChem* **2011**, *4*, 185−190.

(4) Pelaez, M.; Nolan, N. T.; Pillai, S. C.; Seery, M. K.; Falaras, P.; Kontos, A. G.; Byrne, J. A.; O'Shea, K.; Entezari, M. H.; Dionysiou, D. D. A Review on the Visible Light Active Titanium Dioxide Photocatalysts for Environmental Applications. *Appl. Catal., B* **2012**, *125*, 331−349.

(5) Gong, J.; Liang, J.; Sumathy, K. Review on Dye-sensitized Solar Cells (DSSCs): Fundamental Concepts and Novel Materials. *Renewable Sustainable Energy Rev.* **2012**, *16*, 5848−5860.

(6) Goodenough, J. B.; Park, K.-S. The Li-Ion Rechargeable Battery: A Perspective. *J. Am. Chem. Soc.* **2013**, *135*, 1167−1176.

(7) Choudhary, S.; Upadhyay, S.; Kumar, P.; Singh, N.; Satsangi, V. R.; Shrivastav, R.; Dass, S. Nanostructured Bilayered Thin Films in Photoelectrochemical Water Splitting − A Review. *Int. J. Hydrogen Energy* **2012**, *37*, 18713−18730.

(8) Brillet, J.; Yum, J.-H.; Cornuz, M.; Hisatomi, T.; Solarska, R.; Augustynski, J.; Grätzel, M.; Sivula, K. Highly Efficient Water Splitting by a Dual-absorber Tandem Cell. *Nat. Photonics* **2012**, *6*, 824−828.

(9) Murphy, A. B.; Barnes, P. R. F.; Randeniya, L. K.; Plumb, I. C.; Grey, I. E.; Horne, M. D.; Glasscock, J. A. Efficiency of Solar Water Splitting Using Semiconductor Electrodes. *Int. J. Hydrogen Energy* **2006**, *31*, 1999−2017.

(10) Pendlebury, S. R.; Barroso, M.; Cowan, A. J.; Sivula, K.; Tang, J.; Grätzel, M.; Klug, D.; Durrant, J. R. Dynamics of Photogenerated Holes in Nanocrystalline α-Fe_2O_3 Electrodes for Water Oxidation Probed by Transient Absorption Spectroscopy. *Chem. Commun.* **2011**, *47*, 716−718.

DOI: 10.1021/acsami.5b05914
ACS Appl. Mater. Interfaces 2015, 7, 20292−20303

(11) Walter, M. G.; Warren, E. L.; McKone, J. R.; Boettcher, S. W.; Mi, Q.; Santori, E. A.; Lewis, N. S. Solar Water Splitting Cells. *Chem. Rev.* **2010**, *110*, 6446−6473.
(12) Formal, F. L.; Tetreault, N.; Cornuz, M.; Moehl, T.; Grätzel, M.; Sivula, K. Passivating Surface States on Water Splitting Hematite Photoanodes with Alumina Overlayers. *Chem. Sci.* **2011**, *2*, 737−743.
(13) Liao, P.; Keith, J. A.; Carter, E. A. Water Oxidation on Pure and Doped Hematite (0001) Surfaces: Prediction of Co and Ni as Effective Dopants for Electrocatalysis. *J. Am. Chem. Soc.* **2012**, *134*, 13296−13309.
(14) (a) Reyes-Gil, K. R.; Robinson, D. B. WO_3-Enhanced TiO_2 Nanotube Photoanodes for Solar Water Splitting with Simultaneous Wastewater Treatment. *ACS Appl. Mater. Interfaces* **2013**, *5*, 12400−12410.
(15) Bignozzi, C. A.; Caramori, S.; Cristino, V.; Argazzi, R.; Meda, L.; Tacca, A. Nanostructured Photoelectrodes Based on WO_3: Applications to Photooxidation of Aqueous Electrolytes. *Chem. Soc. Rev.* **2013**, *42*, 2228−2246.
(16) Nozik, A. J. Photoelectrolysis of Water Using Semiconducting TiO_2 Crystals. *Nature* **1975**, *257*, 383−386.
(17) Bickley, R. I.; Vishwanathan, V. Photocatalytically Induced Fixation of Molecular Nitrogen by Near UV Radiation. *Nature* **1979**, *280*, 306−308.
(18) Balapanuru, J.; Chiu, G.; Su, C.; Zhou, N.; Hai, Z.; Xu, Q. -h.; Loh, K. P. Photoactive PDI−Cobalt Complex Immobilized on Reduced Graphene Oxide for Photoelectrochemical Water Splitting. *ACS Appl. Mater. Interfaces* **2015**, *7*, 880−886.
(19) Shi, X.; Zhang, K.; Shin, K.; Ma, M.; Kwon, J.; Choi, I. T.; Kim, J. K.; Kim, H. K.; Wang, D. H.; Park, J. H. Unassisted Photoelectrochemical Water Splitting Beyond 5.7% Solar-to-hydrogen Conversion Efficiency by a Wireless Monolithic Photoanode/Dye-sensitised Solar Cell Tandem Device. *Nano Energy* **2015**, *13*, 182−191.
(20) Hartmann, P.; Lee, D.-K.; Smarsly, B. M.; Janek, J. Mesoporous TiO_2: Comparison of Classical Sol−Gel and Nanoparticle Based Photoelectrodes for the Water Splitting Reaction. *ACS Nano* **2010**, *4*, 3147−3154.
(21) Gan, J.; Lu, X.; Rajeeva, B. B.; Menz, R.; Tong, Y.; Zheng, Y. Efficient Photoelectrochemical Water Oxidation over Hydrogen-Reduced Nanoporous $BiVO_4$ with Ni−Bi Electrocatalyst. *Chem. Sus. Chem.* **2015**, in press.
(22) Dong, X.; Tao, J.; Li, Y.; Zhu, H. Oriented Single Crystalline TiO_2 Nano-pillar Arrays Directly Grown on Titanium Substrate in Tetramethylammonium Hydroxide Solution. *Appl. Surf. Sci.* **2010**, *256*, 2532−2538.
(23) Kim, J. Y.; Choi, S. B.; Kim, D. W.; Lee, S.; Jung, H. S.; Lee, J.-K.; Hong, K. S. Surfactant-Assisted Shape Evolution of Thermally Synthesized TiO_2 Nanocrystals and Their Applications to Efficient Photoelectrodes. *Langmuir* **2008**, *24*, 4316−4319.
(24) Zhang, P.; Gao, L.; Song, X.; Sun, J. Micro- and Nanostructures of Photoelectrodes for Solar-driven Water Splitting. *Adv. Mater.* **2015**, *27*, 562−568.
(25) Tiwana, P.; Docampo, P.; Johnston, M. B.; Snaith, H. J.; Herz, L. M. Electron Mobility and Injection Dynamics in Mesoporous ZnO, SnO_2, and TiO_2 Films Used in Dye-Sensitized Solar Cells. *ACS Nano* **2011**, *5*, 5158−5166.
(26) Helander, M. G.; Greiner, M. T.; Wang, Z. B.; Tang, W. M. Work Function of Fluorine Doped Tin Oxide. *J. Vac. Sci. Technol., A* **2011**, *29*, 011019.
(27) Nie, A.; Liu, J.; Li, Q.; Cheng, Y.; Dong, C.; Zhou, W.; Wang, P.; Wang, Q.; Yang, Y.; Zhu, Y.; Zeng, Y.; Wang, H. Epitaxial TiO_2/SnO_2 Core−shell Heterostructure by Atomic Layer Deposition. *J. Mater. Chem.* **2012**, *22*, 10665−10671.
(28) Gao, C.; Zhang, Z.; Li, X.; Chen, L.; Wang, Y.; He, Y.; Teng, F.; Zhou, J.; Han, W.; Xie, E. Synergistic Effects in Three-dimensional $SnO_2/TiO_2/CdS$ Multi-heterojunction Structure for Highly Efficient Photoelectrochemical Hydrogen Production. *Sol. Energy Mater. Sol. Cells* **2015**, *141*, 101−107.
(29) Radecka, R.; Wnuk, A.; Trenczek-Zajac, A.; Schneider, K.; Zakrzewska, K. TiO_2/SnO_2 Nanotubes for Hydrogen Generation by Photoelectrochemical Water Splitting. *Int. J. Hydrogen Energy* **2015**, *40*, 841−851.
(30) Liu, Z.; Sun, D. D.; Guo, P.; Leckie, J. O. An Efficient Bicomponent TiO_2/SnO_2 Nanofiber Photocatalyst Fabricated by Electrospinning with a Side-by-side Dual Spinneret Method. *Nano Lett.* **2007**, *7*, 1081−1085.
(31) Cordova, I. A.; Peng, Q.; Ferrall, I. L.; Rieth, A. J.; Hoertz, P. G.; Glass, J. T. Enhanced Photoelectrochemical Water Oxidation via Atomic Layer Deposition of TiO_2 on Fluorine-doped Tin Oxide Nanoparticle Films. *Nanoscale* **2015**, *7*, 8584−8592.
(32) Wang, T.; Luo, Z.; Li, C.; Gong, J. Controllable Fabrication of Nanostructured Materials for Photoelectrochemical Water Splitting via Atomic Layer Deposition. *Chem. Soc. Rev.* **2014**, *43*, 7469−7484.
(33) Zhou, M.; Bao, J.; Xu, Y.; Zhang, J.; Xie, J.; Guan, M.; Wang, C.; Wen, L.; Lei, Y.; Xie, Y. Photoelectrodes Based upon Mo: $BiVO_4$ Inverse Opals for Photoelectrochemical Water Splitting. *ACS Nano* **2014**, *8*, 7088−7098.
(34) Cao, Y.; Wang, Y.; Zhu, Y.; Chen, H.; Li, Z.; Ding, J.; Chi, Y. Fabrication of Anatase Titania Inverse Opal Films Using Polystyrene Templates. *Superlattices Microstruct.* **2006**, *40*, 155−160.
(35) Lanata, M.; Cherchi, M.; Zappettini, A.; Pietralunga, S. M.; Martinelli, M. Titania Inverse Opals for Infrared Optical Applications. *Opt. Mater.* **2001**, *17*, 11−14.
(36) Schroden, R. C.; Al-Daous, M.; Blanford, C. F.; Stein, A. Optical Properties of Inverse Opal Photonic Crystals. *Chem. Mater.* **2002**, *14*, 3305−3315.
(37) Lee, H. S.; Kubrin, R.; Zierold, R.; Petrov, A. Y.; Nielsch, K.; Schneider, G. A.; Eich, M. Photonic Properties of Titania Inverse Opal Heterostructures. *Opt. Mater. Express* **2013**, *3*, 1007−1019.
(38) Zamani, R.; Fiz, R.; Pan, J.; Fischer, T.; Mathur, S.; Morante, J. R.; Arbiol, J. Oxide−oxide Nanojunctions in Coaxial SnO_2/TiO_2, SnO_2/V_2O_3 and $SnO_2/(Ti0.5V0.5)_2O_3$ Nanowire Heterostructures. *CrystEngComm* **2013**, *15*, 4532−4539.
(39) Hanaor, D. A. H.; Sorrell, C. C. Review of the Anatase to Rutile Phase Transformation. *J. Mater. Sci.* **2011**, *46*, 855−874.
(40) Dou, M.; Persson, C. Comparative Study of Rutile and Anatase SnO_2 and TiO_2: Band-edge Structures, Dielectric Functions, and Polaron Effects. *J. Appl. Phys.* **2013**, *113*, 083703.
(41) Lazzeri, M.; Selloni, A. Stress-Driven Reconstruction of an Oxide Surface: The Anatase TiO_2 (001)−(1 × 4) Surface. *Phys. Rev. Lett.* **2001**, *87*, 266105. Toledo-Antonio, J. A.; Pedraza, F.; Bokhimi, X. The Effect of Doping Low Temperature Rutile with Tin. *J. New Mater. Electrochem. Systems* **2005**, *8*, 85−90.
(42) Phuan, Y. W.; Chong, M. N.; Zhu, T.; Yong, S.-T.; Chan, E. S. Effects of Annealing Temperature on the Physicochemical, Optical and Photoelectrochemical Properties of Nanostructured Hematite Thin Films Prepared via Electrodeposition Method. *Mater. Res. Bull.* **2015**, *69*, 71−77.
(43) Ishii, M.; Harada, M.; Tsukigase, A.; Nakamura, H. Three-dimensional Structure Analysis of Opaline Photonic Crystals by Angle-resolved Reflection Spectroscopy. *J. Opt. A: Pure Appl. Opt.* **2007**, *9*, S372.
(44) Lee, H.-Y.; Yao, T. Design and Evaluation of Omnidirectional One-dimensional Photonic Crystals. *J. Appl. Phys.* **2003**, *93*, 819.
(45) Lee, H. Y.; Jang, S. J.; Kim, E. S.; Chung, H. B. Polarization Dependence of Photoinduced Birefringence in Chalcogenide Thin Film. *Jpn. J. Appl. Phys.* **2001**, *40*, 3965−3968.
(46) Gurunathan, K.; Maruthamuthu, P.; Sastri, M. V. C. Photocatalytic Hydrogen Production by Dye-sensitized Pt/SnO_2 and $Pt/SnO_2/RuO_2$ in Aqueous Methyl Viologen Solution. *Int. J. Hydrogen Energy* **1997**, *22*, 57−62.
(47) Li, J.; Qiu, Y.; Wei, Z.; Lin, Q.; Zhang, Q.; Yan, K.; Chen, H.; Xiao, S.; Fan, Z.; Yang, S. A Three-Dimensional Hexagonal Fluorine-doped Tin Oxide Nanocone Array: a Superior Light Harvesting Electrode for High Performance Photoelectrochemical Water Splitting. *Energy Environ. Sci.* **2014**, *7*, 3651−3658.
(48) Tacca, A.; Meda, L.; Marra, G.; Savoini, A.; Caramori, S.; Cristino, V.; Bisquert, J. Photoanodes Based on Nanostructured WO_3 for Water Splitting. *ChemPhysChem* **2012**, *13*, 3025−3034.

DOI: 10.1021/acsami.5b05914
ACS Appl. Mater. Interfaces 2015, 7, 20292−20303

(49) Kanan, M.W.; Nocera, D. G. In Situ Formation of an Oxygen-Evolving Catalyst in Neutral Water Containing Phosphate and Co^{2+}. *Science* **2008**, *321*, 1072−1075.
(50) Seabold, J. A.; Choi, K. S. Efficient and Stable Photo-oxidation of Water by a Bismuth Vanadate Photoanode Coupled with an Iron Oxyhydroxide Oxygen Evolution Catalyst. *J. Am. Chem. Soc.* **2012**, *134*, 2186−2192.
(51) Wang, H.; Kalytchuk, S.; Yang, H.; He, L.; Hu, C.; Teoh, W. Y.; Rogach, A. L. Hierarchical Growth of SnO_2 Nanostructured Films on FTO Substrates: Structural Defects Induced bu Sn(II) Self-Doping and their Effects on Optical and Photoelectrochemical Properties. *Nanoscale* **2014**, *6*, 6084−6091.
(52) Jia, B.; Jia, W.; Ma, Y.; Wu, X.; Qu, F. SnO_2 Core-shell Microspheres with Excellent Photocatalytic Properties. *Sci. Adv. Mater.* **2012**, *4*, 702−707.
(53) Chen, Z.; Jaramillo, T. F.; Deutsch, T. G.; Kleiman-Shwarsctein, A.; Forman, A. F.; Gaillar, N.; Garland, R.; Takanabe, K.; Heske, C.; Sunkara, M.; MaFarland, E. W.; Domen, K.; Miller, E. L.; Turner, J. A.; Dinh, H. N. Accelerating Materials Development for Photoelectrochemical Hydrogen Production: Standards for Methods, Definitions, and Reporting Protocols. *J. Mater. Res.* **2010**, *25*, 3−16.
(54) (a) Mali, S. S.; Shim, C. S.; Park, H. K.; Heo, J.; Patil, P. S.; Hong, C. K. Ultrathin Atomic Layer Deposited TiO_2 for Surface Passivation of Hydrothermally Grown 1D TiO_2 Nanorod Arrays for Efficient Solid State Perovskite Solar Cells. *Chem. Mater.* **2015**, *27*, 1541−1551.
(55) Luo, J.; Karuturi, S. K.; Liu, L.; Su, L. T.; Tok, A. Y.; Fan, H. J. Homogeneous Photosensitization of Complex TiO_2 Nanostructures for Efficient Solar Energy Conversion. *Sci. Rep.* **2012**, *2*, 451.
(56) Cheng, C.; Ren, W.; Zhang, H. 3D TiO_2/SnO_2 Hierarchically Branched Nanowires on Transparent FTO Substrate as Photoanode for Efficient Water Splitting. *Nano Energy* **2014**, *5*, 132−138.
(57) Vincent, A. The Nature of Semiconductivity in Polycrystalline Tin Oxide. *J. Electrochem. Soc.* **1972**, *119*, 515−518.
(58) Shin, S. W.; Lee, J. Y.; Ahn, K.-S.; Kang, S. H.; Kim, J. H. Visible Light Absorbing TiO_2 Nanotube Arrays by Sulfur Treatment for Photoelectrochemical Water Splitting. *J. Phys. Chem. C* **2015**, *119*, 13375−13383.
(59) Kang, S. H.; Kim, J.-Y.; Kim, Y.; Kim, H. S.; Sung, Y.-E. Surface Modification of Stretched TiO_2 Nanotubes for Solid-State Dye-Sensitized Solar Cells. *J. Phys. Chem. C* **2007**, *111*, 9614−9623.
(60) Leonard, K. C.; Nam, K. M.; Lee, H. C.; Kang, S. H.; Park, H. S.; Bard, A. J. $ZnWO_4/WO_3$ Composite for Improving Photoelectrochemical Water Oxidation. *J. Phys. Chem. C* **2013**, *117*, 15901−15910.
(61) Kim, H. S.; Nguyen, D. T.; Shin, E.-C.; Lee, J.-S.; Lee, S. K.; Ahn, K.-S.; Kang, S. H. Bifunctional Doping Effect on the TiO_2 Nanowires for Photoelectrochemical Water Splitting. *Electrochim. Acta* **2013**, *114*, 159−164.
(62) Turner, J. A. Energetics of the Semiconductor-electrolyte Interface. *J. Chem. Educ.* **1983**, *60*, 327−329.

DOI: 10.1021/acsami.5b05914
ACS Appl. Mater. Interfaces 2015, 7, 20292−20303